JOURNAL OF GEOPHYSICAL RESEARCH: SPACE PHYSICS, VOL. 118, 1635–1650, doi:10.1002/jgra.50221, 2013

CRCM + BATS-R-US two-way coupling

A. Glocer,[1] M. Fok,[1] X. Meng,[2] G. Toth,[2] N. Buzulukova,[3,4] S. Chen,[5] and K. Lin[1]

Received 18 December 2012; revised 19 February 2013; accepted 5 March 2013; published 30 April 2013.

[1] We present the coupling methodology and validation of a fully coupled inner and global magnetosphere code using the infrastructure provided by the Space Weather Modeling Framework (SWMF). In this model, the Comprehensive Ring Current Model (CRCM) represents the inner magnetosphere, while the Block-Adaptive-Tree Solar-Wind Roe-Type Upwind Scheme (BATS-R-US) represents the global magnetosphere. The combined model is a global magnetospheric code with a realistic ring current and consistent electric and magnetic fields. The computational performance of the model was improved to surpass real-time execution by the use of the Message Passing Interface (MPI) to parallelize the CRCM. Initial simulations under steady driving found that the coupled model resulted in a higher pressure in the inner magnetosphere and an inflated closed field-line region as compared to simulations without inner-magnetosphere coupling. Our validation effort was split into two studies. The first study examined the ability of the model to reproduce Dst for a range of events from the Geospace Environment Modeling (GEM) Dst Challenge. It also investigated the possibility of a baseline shift and compared two approaches to calculating Dst from the model. We found that the model did a reasonable job predicting Dst and Sym-H according to our two metrics of prediction efficiency and predicted yield. The second study focused on the specific case of the 22 July 2009 moderate geomagnetic storm. In this study, we directly compare model predictions and observations for Dst, THEMIS energy spectragrams, TWINS ENA images, and GOES 11 and 12 magnetometer data. The model did an adequate job reproducing trends in the data. Moreover, we found that composition can have a large effect on the result.

Citation: Glocer, A., M. Fok, X. Meng, G. Toth, N. Buzulukova, S. Chen, and K. Lin (2013), CRCM + BATS-R-US two-way coupling, *J. Geophys. Res. Space Physics*, *118*, 1635–1650, doi:10.1002/jgra.50221.

1. Introduction

[2] The near-Earth space environment can be thought of as a multiscale system in which different regions have different characteristic lengths, energies, and processes. As a result, different regions are typically modeled by tailored modeling approaches. Combining these disparate approaches, either through reusable and configurable frameworks or by ad hoc model coupling, enables these regions to be studied in concert [*Tóth et al.*, 2012; *Goodrich et al.*, 2004]. This study focuses on the issue of including the ring current into global models, specifically coupling the Comprehensive Ring Current Model (CRCM) with Block-Adaptive-Tree Solar-Wind Roe-Type Upwind Scheme (BATS-R-US) magnetosphere model through the Space Weather Modeling Framework (SWMF).

[3] The ring current is often modeled using a kinetic approach which solves the bounce-averaged Boltzmann equations. These models break the plasma into different populations, each with its own energy and drift velocity which is the sum of the $E \times B$ and gradient-curvature drifts. One widely used ring current model of this type is the Rice Convection Model (RCM) [*Jaggi and Wolf*, 1973; *Harel et al.*, 1981; *Sazykin*, 2000; *Toffoletto et al.*, 2003]. The RCM calculates a self-consistent electric field based on the ring current pressure distribution. The magnetic field is externally specified. Additionally, each species is described by the energy invariant and the assumption of pitch-angle isotropy.

[4] The Fok Ring Current model [*Fok et al.*, 1995; *Fok and Moore*, 1997] and the Ring Current-Atmosphere Interaction Model (RAM) [*Jordanova et al.*, 1994; *Liemohn et al.*, 1999] model the ring current by solving the

[1]Geospace Physics Laboratory, NASA Goddard Space Flight Center, Greenbelt, Maryland, USA.
[2]Department of Atmospheric Oceanic and Space Science, University of Michigan, Ann Arbor, Michigan, USA.
[3]Department of Astronomy, University of Maryland, College Park, Maryland, USA.
[4]CRESST and Geospace Physics Laboratory, NASA Goddard Space Flight Center, Greenbelt, Maryland, USA.
[5]Universities Space Research Association (USRA), Columbia, Maryland, USA.

Corresponding author: A. Glocer, Geospace Physics Laboratory, NASA Goddard Space Flight Center, Greenbelt, MD, USA. (alex.glocer-1@nasa.gov)

2169-9380/13/10.1002/jgra.50221

bounce-averaged Boltzmann equation in external magnetic field and electric fields. These models allow for pitch-angle anisotropy by using the first two adiabatic invariants to describe each plasma population. These models were later expanded to include self-consistent electric fields. The Fok Ring Current model with a self-consistent electric field using the RCM approach became the Comprehensive Ring Current Model (CRCM) [*Fok et al.*, 2001]. The RAM code was similarly expanded [*Ridley and Liemohn*, 2002].

[5] These ring current models use many approaches to get around the problem of how to specify the magnetic field. One common method is to use an empirical magnetic field such as that developed by *Tsyganenko and Stern* [1996]. This empirical model was later expanded to include inner magnetospheric magnetic field depressions during storms using Dst as an input [*Tsyganenko and Mukai*, 2003]. This approach has the advantage of being simple to include in ring current models, but they have some important limitations. First, they are representative of average magnetospheric states, not the true configuration at a given time. Second, the magnetic field is still externally specified and may be inconsistent with the ring current plasma pressure.

[6] One approach to get an improved representation of the magnetic field in the inner magnetosphere is to use the ring current pressures and compute the magnetic field configuration that satisfies the force balance equation $\mathbf{J} \times \mathbf{B} = \nabla \cdot \mathbf{P}$. This 3-D force equilibrium approach was taken by *Zaharia et al.* [2006, 2008] in the development of the RAM code with self-consistent magnetic field (RAM-SCB). Their work required input of the boundary conditions at geosynchronous orbit and an empirical specification of the electric field. *Zaharia et al.* [2010] modified this model to run within the SWMF to get the outer boundary conditions from BATS-R-US and electric field from the ionospheric potential solver which combines BATS-R-US currents with ionospheric conductance to determine the potential and hence the electric field. In this way, the electric field and boundary conditions are included, but the lack of feedback to BATS-R-US leaves room for improvement.

[7] Coupling a ring current model with a global MHD model is another approach to get consistent magnetic and electric fields. In this approach, the global MHD model provides the magnetic field in the inner magnetosphere along with outer boundary conditions for the ring current and the ionospheric potential from its interaction with a conducting inner boundary. The ring current model returns ring current pressure (and in some cases density) which is used to improve the inner-magnetosphere portion of the MHD model. Through frequent information exchange, these models are able to get a ring current model with consistent electric and magnetic fields and a global magnetosphere MHD model with a realistic ring current pressure.

[8] This approach has been implemented using the RCM with two MHD codes. *De Zeeuw et al.* [2004] coupled the RCM with BATS-R-US, and *Toffoletto et al.* [2004] and *Pembroke et al.* [2012] coupled the RCM with the Lyon Fedder Mobbary (LFM) code in the manner described above. The coupled model of *De Zeeuw et al.* [2004] has been extensively used since its development. For instance, *Zhang et al.* [2007] used the coupled model to study a moderate storm and compared the results with several in situ measurements. A systematic validation effort of the coupled model was carried out by *Welling and Ridley* [2010]. They simulated 10 space weather events and compared the results against satellite-specific magnetic field, plasma energy-density spectra, density, and temperature to assess the model performance. They found that the model produced large-scale magnetic field features, and density and temperature were well reproduced. *Glocer et al.* [2011] used this model to drive a radiation belt model and found that dipolarization like events occurred with timing close to observations, resulting in energization of radiation belt electrons.

[9] The present study builds on the work of *De Zeeuw et al.* [2004] to couple the CRCM with BATS-R-US using the SWMF infrastructure. Our newly coupled model has two advantageous capabilities. First, the CRCM does not assume pitch-angle isotropy which is important for studying important processes in the inner magnetosphere. Pitch-angle anisotropy is closely related to the growth rate of electromagnetic ion cyclotron waves which are extremely effective at scattering energetic electrons into the loss cone [*Cornwall et al.*, 1970]. Pitch-angle anisotropy is also important for being able to calculate synthetic energetic neutral atoms (ENA) measurements for comparison with missions such as the Two Wide-Angle Imaging Neutral Spectrometer (TWINS) satellites and IMAGE mission [*Buzulukova et al.*, 2010]. Additionally, using the CRCM paves the way for coupling with an anisotropic MHD version of BATS-R-US, which will be detailed in a forthcoming publication. Second, we have used the Message Passing Interface (MPI) library to parallelize the CRCM to get high computational performance. This ability not only allows for very fast computation but also allows for future expansion to high-resolution grids in CRCM without sacrificing performance.

[10] The above advantages of our newly coupled model also hold when comparing to the work of *Pembroke et al.* [2012]. Moreover, we use a parallel field-line tracing algorithm that allows us to efficiently extract magnetic field traces, essential for the coupling, in a manner that scales well to large numbers of computational cells distributed over many processors. Our newly coupled model, however, does not include a plasmasphere where *Pembroke et al.* [2012] includes a static plasmasphere model. The inclusion of a dynamic plasmasphere model is in our future plans, but it is beyond the scope of the present work. Despite these differences, the present work is along similar lines to *Pembroke et al.* [2012] and *De Zeeuw et al.* [2004]. The approaches all seek to combine bounce-averaged kinetic treatments of the ring current with MHD models of the global magnetosphere in order to obtain a more complete picture of the near-Earth space environment.

[11] Finally, we believe the presented coupling scheme allows us to adequately describe electrodynamics of the inner magnetosphere during active times. To prove that, we run the coupled model for a number of storms. We show a comparison between observed and modeled Dst index, as well comparison with THEMIS, GOES, and TWINS ENA data sets.

[12] A detailed description of our modeling set up is provided in section 2, and the event details and results are given in section 3. We summarize our results and discuss our conclusions in section 4.

2. Model Details

[13] The two main models used in this paper are the Comprehensive Ring Current Model (CRCM) and the Block-Adaptive-Tree Solar-Wind Roe-Type Upwind Scheme (BATS-R-US) magnetosphere model. Using these two codes together allows us to consistently model the inner and outer magnetosphere. This section is divided into three parts. First, section 2.1 provides a brief description of the BATS-R-US model. Then a description of the CRCM code is given in section 2.2. Finally, the coupling and improvement of the parallel performance of the models is described in section 2.3.

2.1. BATS-R-US

[14] In this study, the global magnetosphere is represented by the Block-Adaptive-Tree Solar-Wind Roe-Type Upwind Scheme, or BATS-R-US, code. BATS-R-US is typically configured to solve to the ideal MHD equations but is in fact a multiphysics code. Other than ideal MHD, BATS-R-US can solve the semirelativistic [*Gombosi et al.*, 2001], Hall [*Tóth et al.*, 2008], multispecies [*Glocer et al.*, 2009a], and multifluid [*Glocer et al.*, 2009b] MHD equations. The present study primarily uses BATS-R-US configured to solve the ideal MHD equations. Explicit, implicit, and point-implicit time-stepping are all available. Several total variation diminishing schemes are implemented with a finite volume discretization on block-adaptive grids of both Cartesian and non-Cartesian geometries [*Ma et al.*, 2007; *Stout et al.*, 1997; *Gombosi et al.*, 2001; *Tóth et al.*, 2006, 2008, 2012].

[15] In this study, we use a Cartesian grid. The computational domain of the magnetosphere model extends from 32 R_E upstream to 224 R_E downstream of the planet and 64 R_E to the sides. The inner boundary is a sphere of radius 2.5 R_E centered on the Earth. The grid resolution varies from 1/8 R_E in most of the inner magnetosphere to 4 R_E near the outer edges of the simulation domain. The use of higher resolution in the inner magnetosphere is needed for the accurate field-line tracing required by the inner-magnetosphere coupling. We set the solar-wind conditions upstream of the planet using measurements by the ACE satellite.

[16] The BATS-R-US global magnetosphere model interacts with models representing other physical domains through the Space Weather Modeling Framework (SWMF) (see *Tóth et al.* [2005]; *Tóth et al.* [2012] for details). In the configuration used for this study, the BATS-R-US inner boundary interacts with an ionosphere model represented by a 2-D height-integrated conductance model and potential solver [*Ridley et al.*, 2004]. The SWMF also provides the coupling framework through which we couple the CRCM model (see section 2.3).

2.2. CRCM

[17] The Comprehensive Ring Current Model (CRCM) [*Fok et al.*, 2001] provides a description of the inner-magnetosphere ring current electrons and ions. The temporal and spatial variation is found by solving the bounce-averaged Boltzmann transport equation [*Fok and Moore*, 1997] given by the following:

$$\frac{\partial f_s}{\partial t} + \langle \dot{\lambda}_i \rangle \frac{\partial f_s}{\partial \lambda_i} + \langle \dot{\phi}_i \rangle \frac{\partial f_s}{\partial \phi_i} = \left(\frac{\delta f_s}{\delta t} \right)_{\text{Loss}} \quad (1)$$

where $f_s = f_s(t, \lambda, \phi, M, K)$ is the field-line averaged distribution function of a species s. The magnetic latitude and magnetic local time (MLT) are represented by λ and ϕ, and the relativistic magnetic moment is given by M. $K = J/\sqrt{8m_0 M}$, with J representing the second adiabatic invariant. The right-hand side of the equation represents the loss terms due to scattering into the loss-cone and charge exchange. Coulomb losses and wave diffusion are also included in the model [*Fok et al.*, 1996]. The CRCM grid is defined by the ionospheric foot point of the field line. The simulation domain is further restricted to the region of closed field lines, extending no further than 15 Earth radii from the center of the planet.

[18] The CRCM differs from the RCM (the only other two-way coupled inner-magnetosphere model) in that it provides both pitch-angle and energy information. The inclusion of pitch-angle information allows for a broader study of physical processes, including wave-particle interactions and loss processes that lead to scattering into the loss cone. Additionally, the pitch-angle information is needed for the ENA estimations carried out in section 3.

[19] *Buzulukova et al.* [2010] has taken the first steps toward coupling the CRCM with the BATS-R-US code. This work has established one-way coupling where magnetic field information is provided to the CRCM from BATS-R-US, but inner magnetospheric pressure is not passed back. The present work builds on the past work of *Buzulukova et al.* [2010] by completing the full two-way coupling.

2.3. Coupling

[20] To couple the CRCM and BATS-R-US models together, we take advantage of existing infrastructure in the Space Weather Modeling Framework (SWMF) for inner-magnetosphere coupling put in place by *De Zeeuw et al.* [2004]; the ability to reuse coupling infrastructure for multiple modeling components is a key advantage of the framework approach. The details of the coupling and some computational improvements are described in this section.

[21] The information flows between the models can be described as follows. Magnetic field-line traces whose foot points correspond to the CRCM grid are extracted from the BATS-R-US model using an efficient parallel field-line tracing algorithm described by *Glocer et al.* [2009c]. Those field-line traces are passed to the CRCM model along with equatorial mass density and pressure at the CRCM outer boundary, typically near 10 R_E on the nightside. The CRCM also takes the ionospheric potential calculated by the interaction of BATS-R-US and a height-integrated conductance model and potential solver [*Ridley et al.*, 2004]. The CRCM then calculates the ring current fluxes and determines the density and pressure. The density and pressure at the minimum magnetic field location along the field line are then fed back to BATS-R-US and used to nudge the BATS-R-US values in the inner magnetosphere. We note that the CRCM feedback creates pressure-driven region 2 field-aligned currents in BATS-R-US that are included in the currents passed to the height-integrated potential solver. In other words, it is the BATS-R-US potential solver that is used [*Ridley et al.*, 2004], but the currents account for both BATS-R-US and CRCM contributions.

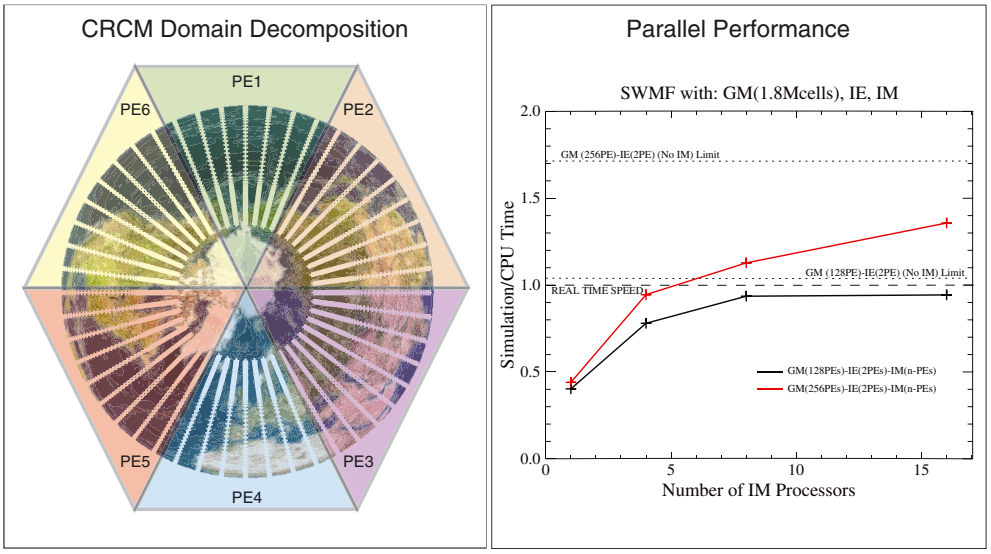

Figure 1. A description of the parallelization and performance of the coupled CRCM model. The schematic on the left shows how the CRCM ionospheric grid is domain decomposed onto six processors. The plot on the right presents the parallel scaling performance of the coupled model as the number of processors dedicated to CRCM is increased.

[22] The application of the CRCM density and pressure in BATS-R-US is done in the following manner. BATS-R-US must find (or determine the nonexistence of) the ionospheric foot point of every point in the magnetosphere domain; the parallel field-line tracing algorithm is used again here. The CRCM density and pressure (at the minimum B location) is then interpolated to that foot point. Since CRCM allows for pitch-angle anisotropy, the density and pressure it calculates is not necessarily constant along the field line. Varying these values along the field line, however, is not consistent with an equilibrium solution in ideal MHD. Therefore, when applying the CRCM density and pressure in BATS-R-US, we assume them to be constant along the field line. As a result, the density and pressure interpolated to the foot point are taken to be the density and pressure at the corresponding point in the magnetosphere. Rather than overwrite the BATS-R-US density and pressure with the CRCM values, which could introduce numerical instabilities, we create a source term in the continuity and pressure equation that pushes the BATS-R-US values toward the CRCM values over some time τ. For pressure, the source term takes the form

$$\frac{p_C - p_B}{\tau} \tag{2}$$

where p_B is the BATS-R-US pressure and p_C is the CRCM pressure at a given location. The choice of a specific τ is left to the user, but we have found that 20 s seems to work well. An analogous equation is used for the density. All of the information exchange happens on the order of 5–10 s.

[23] We recognize that the assumption of constant pressure along a field line implies an isotropic pitch-angle distribution which is not necessarily the case in CRCM. An alternative possibility is to drop the assumption of constant pressure along the field line. Allowing the pressure to vary in this way, however, is inconsistent with an equilibrium solution in MHD and so this approach is not used. Another possibility is to use anisotropic MHD in BATS-R-US [see *Meng et al.*, 2012], in which case varying the pressure along the field line consistent with the pitch-angle distribution in CRCM would be possible. The implementation of the anisotropic MHD equations in BATS-R-US is still quite new, and so we leave this option to a separate publication. We view holding the pressure constant along the field line a reasonable compromise that allows the coupling to work for ideal, Hall, multifluid, and semirelativistic MHD.

[24] We discovered during our initial tests of the coupled model that simulations with the CRCM model ran much slower than simulations with just BATS-R-US and the ionospheric potential solver. To improve computational efficiency, we parallelized CRCM using the Message Passing Interface (MPI). In particular, we use domain decomposition to divide the CRCM grid in MLT equally among processors. The left panel of Figure 1 presents a schematic view of how the domain is divided. The figure shows the ionospheric CRCM grid (white crosses), and the colored translucent triangles represent the portion of the grid allocated to a given processor. This example shows how the domain is divided among six processors, although any number of processors could be used as long as that number is less than the number of points in MLT. An additional advantage of this model parallelization is that we can choose to increase the grid resolution in the model with only a modest penalty as long as we have extra processors.

[25] To test the performance of the coupled model and the newly parallelized CRCM, we conduct two scaling tests on the NASA Pleiades supercomputer. Both tests use BATS-R-US with 1.8 million cells in the magnetosphere, the ionospheric solver on two processors, and the CRCM on one, four, eight, and 16 processors. The first test has BATS-R-US running on 128 processors, and the second test has BATS-R-US running on 256 processors. The results of the scaling tests are presented in the right panel of Figure 1. The horizontal axis represents the number of inner-magnetosphere (IM) processors used by CRCM, and the vertical axis is the

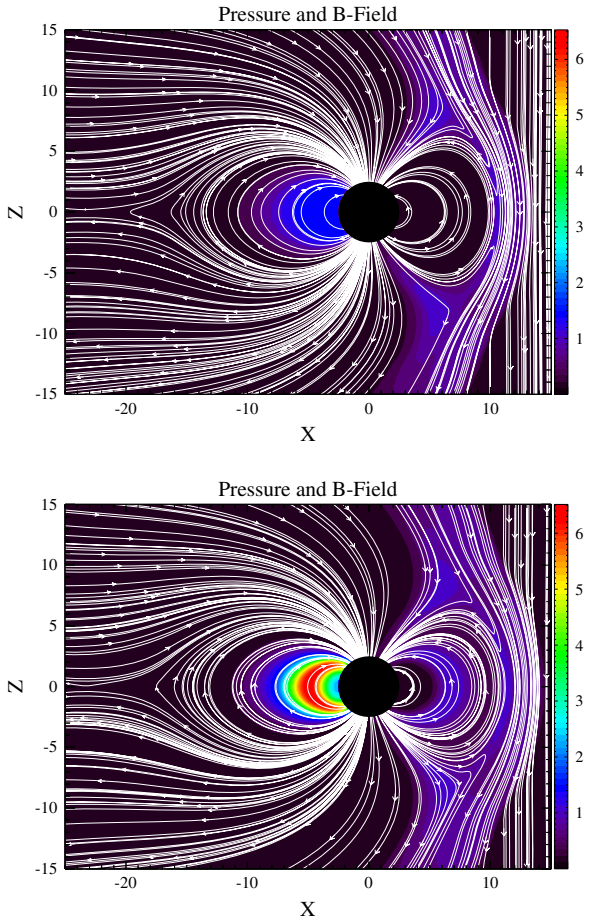

Figure 2. Pressure and magnetic field in the x-z plane with the sun to the right after 12 h of simulation with pure southward IMF and steady solar-wind conditions. The plot on the left does not include coupling with CRCM, while the plot on the right does.

ratio of simulation time to CPU time. The horizontal dashed line at Simulation/CPU Time = 1.0 shows real-time speed. The dotted lines above it show the performance of the model without CRCM for each test case. The first test (black line) shows the coupled model reaching near real-time performance when eight processors are dedicated to CRCM. The lack of further improvement as more processors are added to CRCM is due to having reached the performance level when CRCM is not included minus the overhead costs from the coupling. The second case (red line) shows that real-time performance is surpassed when eight processors are dedicated to CRCM, and the model performance continues to improve as more processors are dedicated to CRCM. Eight processors is a paltry number compared to the number typically used by BATS-R-US so the extra processors needed to get fast performance is not a large burden.

[26] We test the basic effect of two-way coupling with the inner magnetosphere by contrasting two simulations: one with inner-magnetosphere coupling and one without. Our two simulations are run for 12 h with constant southward IMF (B_Z = –5 nT) and steady, typical, solar-wind conditions. For this test, we also align the dipole axis and rotation axis together with the z axis to reduce complexity. Figure 2

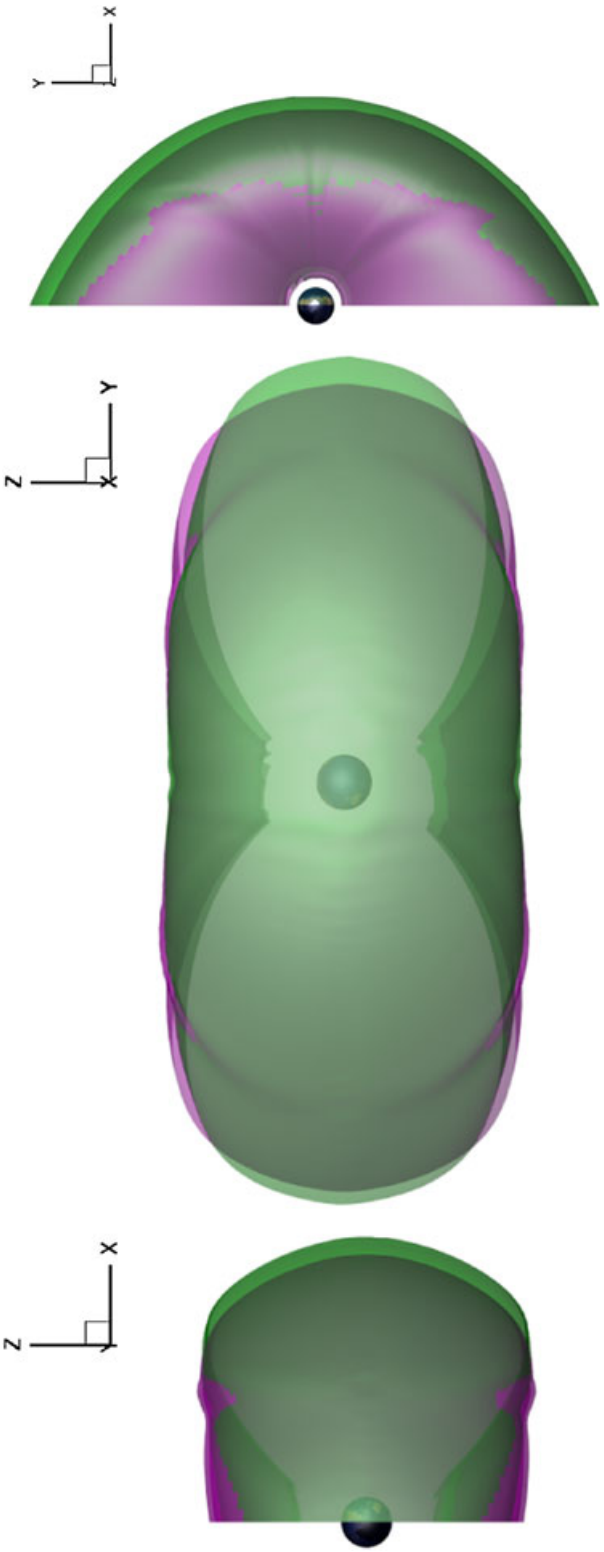

Figure 3. A presentation of the effect of inner-magnetosphere coupling on last closed field-line surface on the dayside in Geocentric Solar Magnetic (GSM) coordinates. The green surface represents the case with inner-magnetosphere coupling, while the purple surface represents the case with no inner-magnetosphere coupling. When inner-magnetosphere coupling is included, the closed field-line surface moves further from the planet.

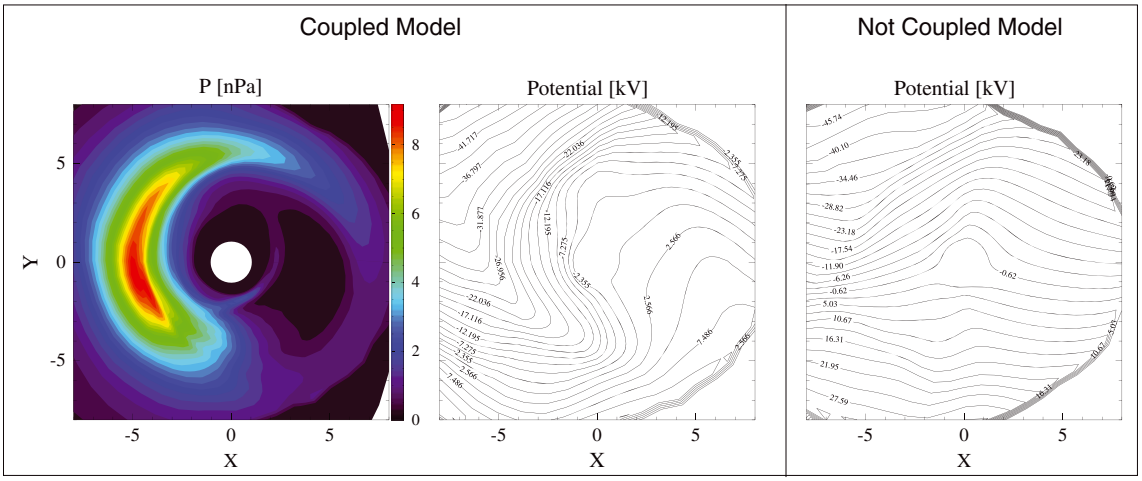

Figure 4. The pressure in the equatorial plane from CRCM (left) and the electric potential mapped to the equatorial plane (middle) at the end of a 12 h coupled simulation with pure southward IMF and steady solar-wind conditions. The potential mapped to the equatorial plane without coupling is shown on the right for comparison.

shows the pressure and magnetic field in the x-z plane for this test. The plot on the left does not include inner-magnetosphere coupling, while the plot on the right does include inner-magnetosphere coupling. The figure shows that including two-way coupling with CRCM, we get a substantially larger pressure in the inner magnetosphere.

[27] Figure 3 presents the effect of coupling with the inner magnetosphere on the shape of the last closed field-line surface on the dayside. We find this surface in the following manner. First, we select a regular grid of points on the dayside in polar and azimuthal angle. We then find the radial location of the last closed field-line surface corresponding to each polar and azimuthal angle by using a very efficient and precise bisection method. Specifically, for each angle pair we choose two points at different radial distances; one is at 3 R_E, and the other is at 25 R_E. If we restrict the polar angle range to avoid the polar cap, magnetic field lines traced from these two points will have "closed" and "open" topologies. A point is then chosen with a radial distance in the middle of these two points, and the topology of the magnetic field line going through that bisecting point is determined. Based on the topology, we can determine if the radial crossing point of the last closed field-line surface is between the bisecting point and the Earthward boundary or the bisecting point and the anti-Earthward boundary. The bisecting point now becomes a boundary of the interval containing the point on the last closed field-line surface, a new point bisecting that interval is chosen, and the process begins anew. We continue this bisecting approach until the interval shrinks to the desired level of accuracy, 10^{-6} R_E in this case. Repeating the method for each polar and azimuthal angle, we can accurately find the last closed field-line surface.

[28] The green surface represents the case with inner-magnetosphere coupling, while the purple surface represents the case without inner-magnetosphere coupling. Clearly, including two-way coupling with the inner magnetosphere causes the surface formed by the last closed field line to stand further away from the planet with a slight dawn dusk asymmetry. This is because, as seen in Figure 2, including inner-magnetosphere coupling increases the thermal pressure in the inner magnetosphere, effectively inflating the closed field-line region. A stronger ring current acts to increase the magnetic field on the dayside and more effectively stand off the solar wind. The asymmetry can be explained by looking at the equatorial pressure distribution presented in the left plot of Figure 4. The pressure is seen to have a similar dawn dusk asymmetry. We also note that the electric potential in the equatorial plane (middle) is consistent with self-consistent electric field calculations with the uncoupled CRCM. Comparing this potential to the potential pattern without a ring current (right) shows that inclusion of the ring current leads to increased shielding and a skewing of the potential.

3. Results

[29] We apply our newly coupled model in two studies. The first study is presented in section 3.1 and focuses on the ability of the model to calculate Dst in four different events. Dst is a useful quantity for validating our coupled model as it is related to the total energy density of the ring current. The second study, presented in section 3.2, is an in-depth study of a single event that looks at the model's ability to reproduce and understand Dst, ion flux, magnetic field, and ENA measurements.

3.1. Study 1: GEM Dst Challenge

[30] The first application of the newly coupled model is the Geospace Environment Modeling (GEM) Dst challenge. This challenge was organized by a focus group of the GEM community to test the ability of various models to produce Dst [*Rastätter et al.*, 2013]. That challenge consists of four events ranging from moderate to super storms. Specifically, the dates of the chosen events are the following:

[31] 1. Event 1: 29 October 2003
[32] 2. Event 2: 12 December 2006
[33] 3. Event 3: 31 August 2001
[34] 4. Event 4: 31 August 2005

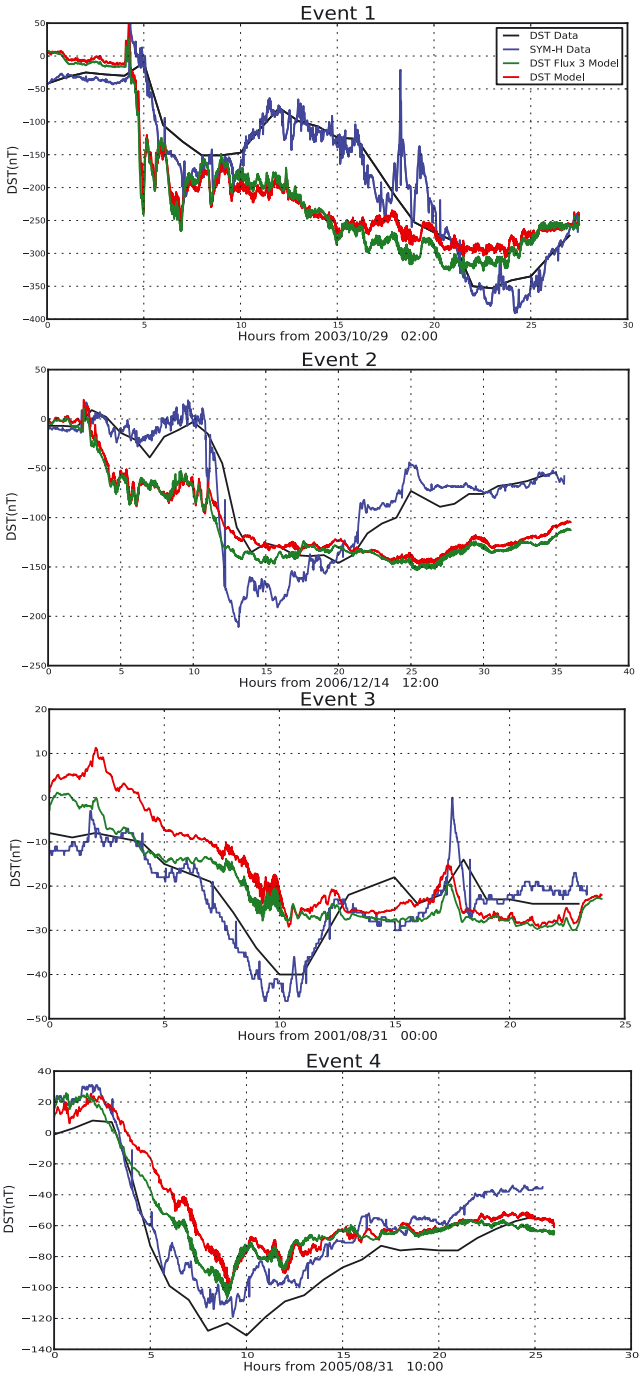

Figure 5. A comparison of modeled Dst with observed Dst (black) and Sym-H (blue) for all four events. Modeled Dst calculated from the Biot-Savart integral is shown in red, and the modeled Dst calculated from taking the average magnetic perturbation on a sphere of radius 3 R_E centered around the Earth is shown in green.

[35] The purpose of this GEM challenge is to objectively test the performance of various models in their ability to predict Dst for a variety of cases. Our primary in using the challenge in this study is to provide an initial validation of our coupled model. Dst is a particularly good parameter to examine as it is directly tied to the ring current energy density through the so-called DPS relationship [*Dessler and Parker*, 1959; *Vasyliunas*, 2006]. Initial results from this study will also be included in the official publication of results from the GEM Challenge. The work here goes beyond what will be published as part of that challenge by including a comparison of synthetic Dst and Sym-H to measured Dst and Sym-H and by comparing two different methods for calculating synthetic Dst and Sym-H.

[36] In this study, we calculate synthetic Dst from the model using two different methods. The first is to determine the perturbation at the center of the Earth by taking the Biot-Savart integral over all cells in the simulation domain. For ease of reference, we will refer to synthetic Dst evaluated in this way as "Dst Model." The second method is to evaluate the average magnetic perturbation over a spherical shell centered around the Earth of radius 3 R_E (chosen since it is close to the inner boundary but not overlapping that boundary). For ease of reference, we will refer to synthetic Dst evaluated using this second method as "Dst Flux 3 Model." These methods should give similar results as both techniques are intended to approximate the magnetic perturbation at the center of the Earth. However, the IMF contributes a uniform magnetic field with no currents inside the computational domain. This contribution is therefore not included in the Biot-Savart integral that is performed inside the computational domain. The Dst Flux 3 Model approach does include this contribution. To illustrate this effect, consider the limiting case where the dipole field of the Earth is switched off. In this case, the entire magnetic perturbation would be due to the IMF. However, this contribution would not be included in the Biot-Savart integration. Averaging the perturbation on the surface of a spherical shell (like the Dst Flux 3 approach) would find the correct perturbation. We also note that choice of radius for the spherical shell in the Dst Flux 3 calculation could potentially be the source of some of the difference.

[37] Figure 5 presents a direct comparison of our modeled Dst to measured Dst and Sym-H. The black and blue lines represent the measured Dst and Sym-H, respectively. The red and green lines are the Dst Model and Dst Flux 3 Model results, respectively. Each panel shows a different event. The *x* axis represents hours from the start of the simulation (starting time is labeled for each case). The *y* axis represents the magnetic perturbation in nanotesla.

[38] To objectively evaluate the ability of the model to replicate each of these cases, we adopt the GEM challenge metrics of prediction efficiency and prediction yield. Prediction yield is defined by the following:

$$\text{PredictionYield} = \frac{\max(\text{Dst}_{\text{model}}) - \min(\text{Dst}_{\text{model}})}{\max(\text{Dst}_{\text{measured}}) - \min(\text{Dst}_{\text{measured}})} \quad (3)$$

and is a basic measure of the model's ability to reproduce the maximum change in Dst. A value of 1.0 indicates a perfect prediction yield, while values above or below 1.0 indicate an overestimate or underestimate of the maximum change. The prediction efficiency is defined by the following:

$$\text{PredictionEfficiency} = 1.0 - \frac{\langle \text{Dst}_{\text{model}} - \text{Dst}_{\text{measured}} \rangle^2}{\sigma^2_{\text{measured}}} \quad (4)$$

and is a measurement of whether the model error exceeds the variance in the data. A prediction efficiency of 1.0 is a

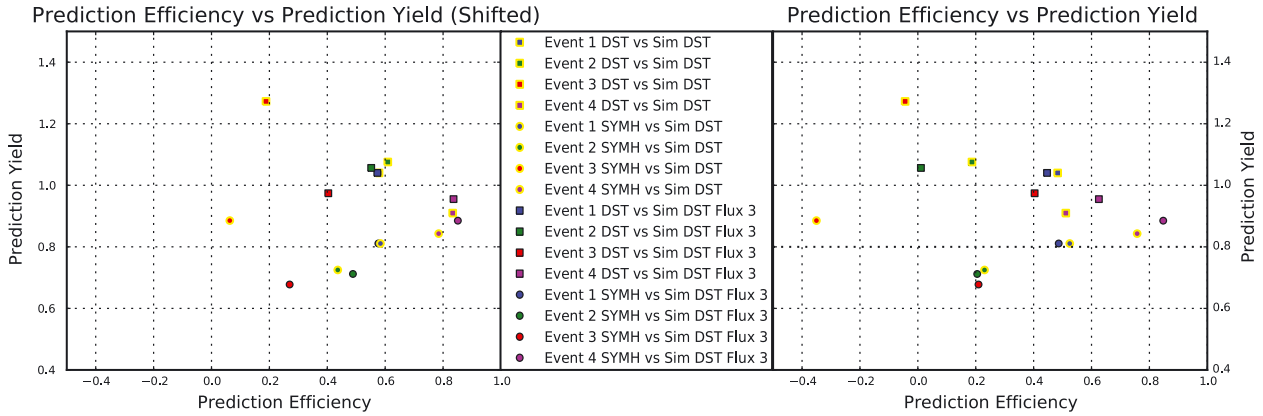

Figure 6. Scatter plots of model performance showing the prediction yield and the prediction efficiency for each event. Skill scores are computed using Dst and Sym-H comparisons for both methods of calculating the Dst perturbations discussed. The plots on the left show the results including a baseline shift, while the plots on the right include no shift.

perfect prediction (no model error). A prediction efficiency of 0.0 indicates that the error is comparable to the variance, and a value less than 0.0 indicates that the error exceeds the variance in the data.

[39] We present the skill scores in Figure 6 using scatter plots with prediction efficiency on the *x* axis and prediction yield on the *y* axis. Each event is color coded: event 1 (blue), event 2 (green), event 3 (red), and event 4 (purple). Hour-averaged Dst comparisons have a square shape, and minute-averaged Sym-H comparisons have a circular shape. Comparisons where the modeled Dst was found using the Biot-Savart integral have a thick yellow border, and cases where the modeled Dst was found by taking the average magnetic perturbation on a surface of radius 3 R_E centered around the Earth have a thin boarder. We further investigate the contribution of a potential baseline shift that may be corrected for in the data but not in the model result. The left panel of Figure 6 shows the result with a shift of no more than $\pm$20 nT that gives the best comparison; the right-hand panel shows the unshifted result.

[40] Examination of the results presented in Figure 6 allows us to draw the following conclusions. First, our modeled results compared with hour-averaged Dst produced a better prediction yield than comparisons with minute-averaged Sym-H. This is likely due to spikes visible in the Sym-H observations that get smoothed out in the Dst observations. Second, the worst prediction efficiency is found for the smallest event (event 3), while the best prediction efficiency is found for event 4 which has a "classic" Dst signature. By "classic" we mean a the Dst exhibits a clear onset, main phase, and recovery. Smaller events, such as event 3, have a much smaller variance than larger events, resulting in larger ratios of error to variance and lower prediction efficiencies. Third, the two methods of calculating synthetic Dst from the model yield similar results in most cases, but the Dst Flux 3 Model approach gives notably better results in event 3. The difference in event 3 is likely due to small changes having a bigger effect on the metrics since the observed variance and observed difference between maximum and minimum values are smaller. Finally, the inclusion of a baseline shift improves the prediction efficiency of the result in all cases; when a baseline shift is included, none of the comparisons have negative prediction efficiency. The magnetic field perturbation is known to be nonzero by as much as 25 nT when Dst is zero [*Sugiura*, 1973; *Langel et al.*, 1980], but the model does not account for this in its calculation; a baseline shift is therefore reasonable.

[41] Overall, our newly coupled model does a reasonable job predicting Dst and Sym-H according to our two metrics. The predictive yield demonstrates that we capture the net change in most cases within 20–30%. A positive prediction efficiency for most cases without the baseline shift, and for all cases with the baseline shift, demonstrates that the error is smaller than the variance in the data. Compared to other global MHD models that also studied these events as part of the GEM Dst modeling challenge (published separately), our model performs quite well. Of course, this study only focuses on one parameter, Dst, but in the next section, we will present a more in-depth case study.

3.2. Study 2: Event Study of 22 July 2009

[42] In our second part of the study, we examine the moderate geomagnetic storm that occurred on 22 July 2009. This event has excellent data coverage from TWINS 1 and 2 satellites, THEMIS satellites, and GOES 11 and 12 magnetometer data; we compare directly to all of these data sets. Moreover, this event was previously studied by *Fok et al.* [2010] using the standalone CRCM model, allowing us to assess the benefits of using a two-way coupled model. In addition to providing validation of the modeling approach, we also use this event study to look at the consequences of ion composition on the model calculation.

[43] Figure 7 presents the geomagnetic indices and solar-wind conditions for this event. The solar-wind speed increased from about 300 km/s at the start of the day to about 450 km/s half way through. The solar-wind density peaks at 50 cm^{-3} at about 3:30 UT before slowly falling back below 10 cm^{-3} at 10:00 UT. The IMF Bz begins at –5 nT and then drops to –15 nT at 3:00 UT. There is a brief northward turning at 5:00 UT, coinciding with a strongly negative By component, before Bz dips again to –15 nT at 7:00 UT. The Dst exhibits a double dip pattern, reaching a minimum of about –80 nT at 6:00 UT and again at 9:00 UT. Two dips

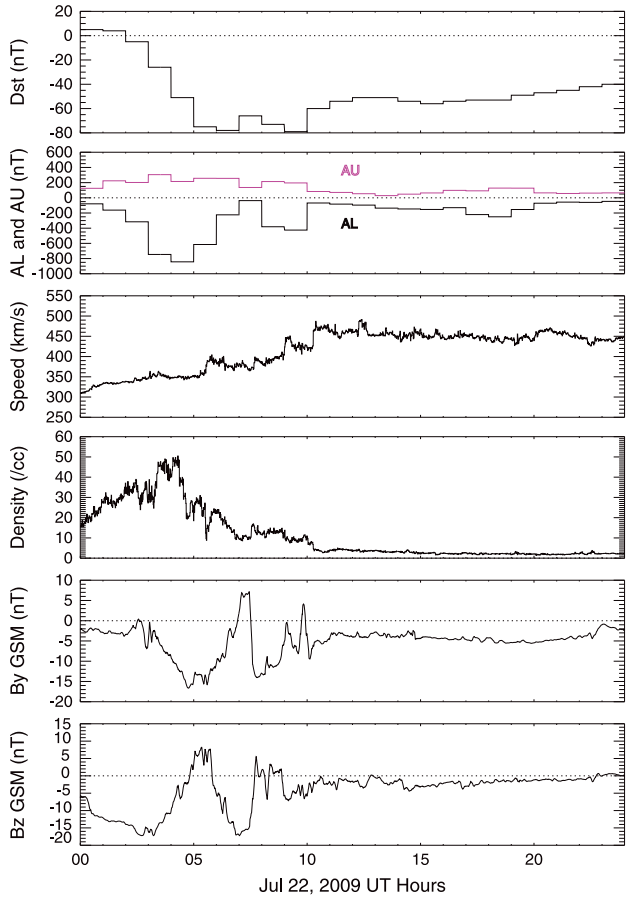

Figure 7. Geomagnetic indices and solar-wind conditions during the moderate storm on 22 July 2009.

in the AL index indicate significant substorm activity during this time.

[44] In this study, we consider the coupled model with two variations of composition. In these cases, we have to make an assumption of the relative composition of the density passed from BATS-R-US to the CRCM outer boundary; in the first case, we assume the composition to be 20% O^+, and in the second case, we assume that the composition is 40% O^+. Both cases further assume that H^+ and O^+ have the same temperature. These assumptions are clearly imperfect, but since we are solving the ideal MHD equations, there is little other choice. In future studies, we may improve on these assumptions by configuring BATS-R-US to solve the multifluid MHD equations [*Glocer et al.*, 2009b, 2009a].

[45] Figure 8 shows how the average composition at geosynchronous orbit varies over the course of the event based on the empirical relationship of *Young et al.* [1982]. The solid black line shows the average O^+/H^+ ratio, while the dotted lines show the extremes of what the relationship could give. Our 20% O^+ case shown in red represents the average expected composition, while the 40% O^+ case shown in purple reflects the upper range of O^+ we could expect. We note that the CRCM outer boundary is further out than 6.6 R_E, and the empirical relationship in the figure is meant to be used only as a guide for what the variation in the composition could be.

[46] Figure 9 presents a comparison of the observed and calculated Dst for the event. The blue line shows the observed Dst. The red color corresponds to the 20% O^+, and the green corresponds to the 40% O^+ case. The solid line and dashed lines distinguish between the two methods for calculating Dst from the simulation as described in the previous section. The case with less O^+ reaches lower Dst values, drops faster than the case with more O^+, and, up until about 10:00 UT, matches the data better. After 10:00 UT, the case with more O^+ appears to be in better agreement. As expected from the empirical relationship of *Young et al.* [1982], the amount of O^+ is expected to vary over the course of the event, so the fixed values we consider for composition may not perform as well as a varying composition.

[47] To understand why increasing O^+ reduces Dst in our simulation, we have to consider the effect on the boundary temperature. At the outer boundary, BATS-R-US provides CRCM with the total mass density and pressure. Based on the relative composition, CRCM converts that total mass density and pressure into number density and temperature. Since O^+ is 16 times heavier than H^+ and we assume that both species have the same temperature, increasing the percentage of O^+ results in larger temperatures. Moreover, higher temperatures mean larger gradient-curvature drifts. The likelihood of a particle at the boundary of the simulation being trapped in the ring current depends on the interplay between the $E \times B$ and gradient-curvature drifts; the larger the gradient-curvature drift is relative to the $E \times B$ drift, the more likely the particle is to hit the magnetopause and be lost. Therefore, increasing the percentage of O^+ on the boundary raises the temperature on the boundary but results in a weaker ring current. This same effect was noted by *Welling et al.* [2011].

[48] It is important to note that H^+ and O^+ do not necessarily share the same temperature and the presence of large quantities of cold O^+ on the boundary could have the opposite effect and increase the ring current strength. This demonstrates a fundamental limitation of using single-fluid MHD in this coupling scheme; single-fluid MHD does not

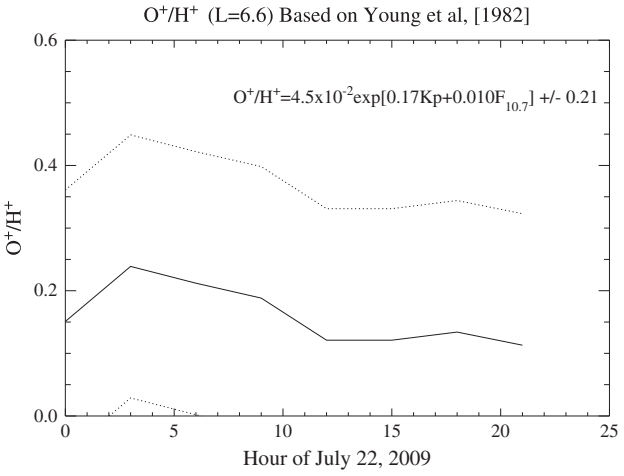

Figure 8. Expected composition at 6.6 R_E based on the formula of *Young et al.* [1982]. The solid line is the average value expected from the formula, and the dashed lines represent the upper and lower ranges from the formula.

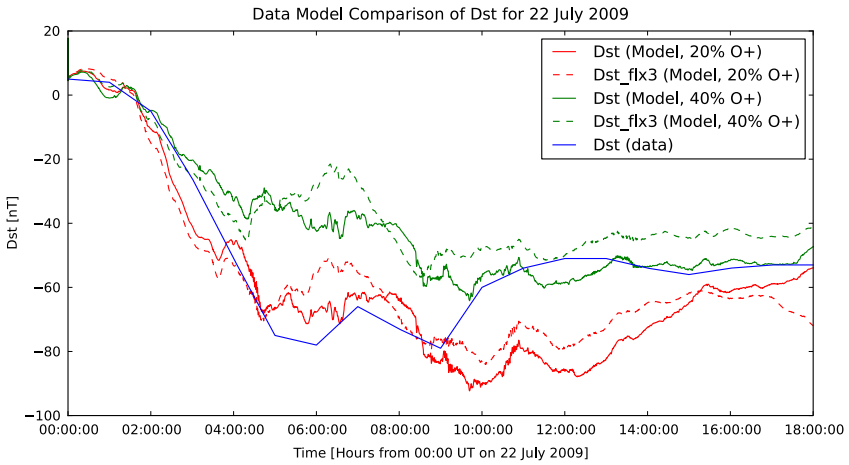

Figure 9. A comparison of observed Dst (blue) with modeled Dst for the low O^+ case (red) and the high O^+ case (green). The solid red and green lines represent modeled Dst calculated by taking a Biot-Savart integral over the entire magnetosphere, while the dashed red and green lines represent the Dst calculated by taking an average perturbation over a sphere of radius 3 R_E centered around the Earth.

provide any information regarding the composition or temperature of the various species, and some assumptions must be made. Those assumptions can significantly alter the ring current which is very sensitive to composition, density, and temperature on the boundary. Therefore, future work must make use of multifluid MHD with an ionospheric source.

[49] Beyond Dst, we can also use satellite observations to validate the ion flux levels predicted by our model. We do this in two ways. First we extract the ion flux along the THEMIS D trajectory as it cuts through the ring current and compare it with the in situ THEMIS D measurements. The THEMIS D trajectory is shown in Figures 10a–10c. This comparison provides a direct comparison of the energy and time distribution of the ion flux but only at a specific spatial and temporal location. To get a more global understanding of the flux, we compare TWINS 1 energetic neutral atom (ENA) observations with synthetic ENA images created from our model. ENAs are formed when hot ring current ions charge exchange with the extended neutral exosphere of the Earth resulting in a hot neutral atom and a cold ion. ENAs therefore provide an indirect observation of the ring current ion flux.

[50] Figure 10 presents a direct comparison of the energy-time spectrogram of the ion differential energy flux from THEMIS D along with the model results extracted along the satellite trajectory (shown in Figures 10a–10c). Figure 10d shows the in situ observations, Figure 10e shows the case with 20% O^+ on the outer boundary, and Figure 10f shows the case with 40% O^+ on the outer boundary. We see that before 11:00 UT, the case with less O^+ has larger fluxes and a broader energy distribution than both the observations and the case with more O^+. We further find that before about 11:00 UT, the case with more O^+ predicts slightly smaller fluxes than the THEMIS D observations, but the peak of the distribution is slightly higher. After about 12:00 UT, on the outbound leg of the satellite orbit, both simulation cases underestimate the flux levels. Despite underestimating the flux, the overall shape of the distribution, including the location of the peak, the notch at about 20 keV, and the increased low energy population below 10 keV, is similar. We also find that the gap in the flux between the inbound and outbound trajectories is smaller in the simulation than in the data. This reduced gap size indicates that the ring current penetrates closer to the Earth in the simulation than it does in reality and also that the shielding is too weak.

[51] Another interesting feature of the comparison in Figure 10 is the ability of the model to reproduce the "nose structure" apparent in the observations. The term "nose structure" was introduced by *Smith and Hoffman* [1974] and is indicative of ions of a particular energy penetrating to lower L-shell than ions of different energies. The formation of nose structures has been previously found to be sensitive to representation of the electric field [e.g., *Buzulukova et al*. 2003; Buzulukova and Vovchenko 2008]. This particular nose structure was also modeled using a self-consistent electric field and empirical magnetic field with the uncoupled version of the CRCM model [*Fok et al.*, 2010]. Our results are qualitatively similar to those with the uncoupled version of the CRCM model, but there are some key differences. The simulated fluxes along the ion trajectories during the outbound trajectory (after 12:00 UT) are stronger in the uncoupled version, and the energy bin that penetrates furthest into the ring current is lower. These differences indicate that the shielding effects in the uncoupled model are stronger than in the coupled model.

[52] The availability of new energetic neutral atom (ENA) observations from the TWINS satellites allows us to evaluate the reasonableness of our modeled ion flux in a global sense. To generate synthetic ENA observations from our simulations, we combine the modeled ion flux and magnetic field with an empirical model of the neutral exosphere. Using an optically thin assumption and knowledge of the spacecraft location and pointing, we can construct line-of-sight integrated images of ENA that can be directly compared to TWINS observations. It is important to note that the CRCM fluxes contain pitch-angle information so the ENA emissions are not assumed to be isotropic.

[53] Figure 11 shows TWINS 1 ENA observations at 13.4 keV (top row) compared to synthetic ENA images for our two composition cases (bottom two rows). Two times

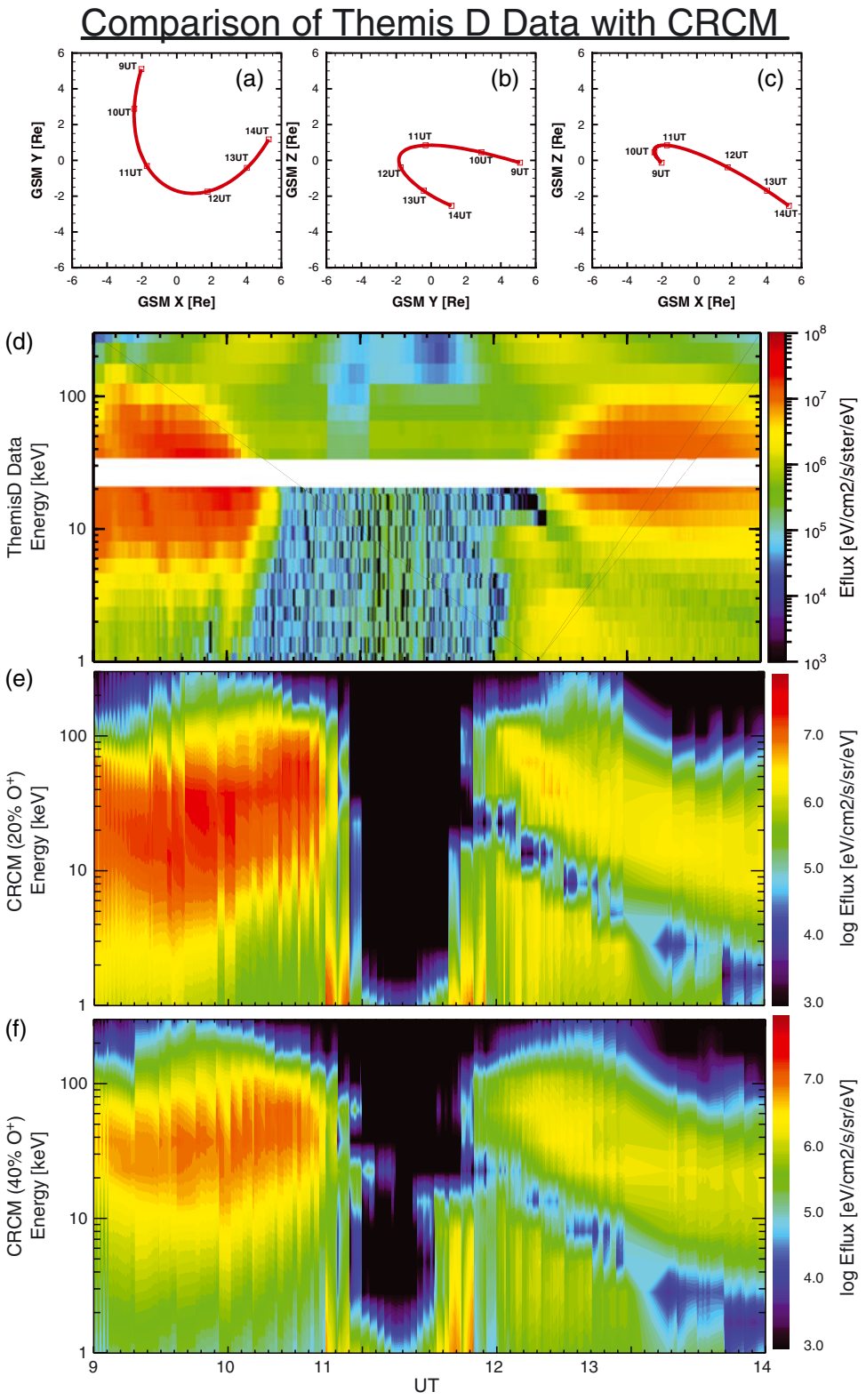

Figure 10. A comparison of THEMIS D differential energy flux data with CRCM results as the satellite cuts through the inner magnetosphere. (a, b, c) The THEMIS D trajectory. (d) The THEMIS D observations, (e) the model results extracted along the satellite trajectory for the low O^+ case, and (f) the model results extracted along the satellite trajectory for the high O^+ case.

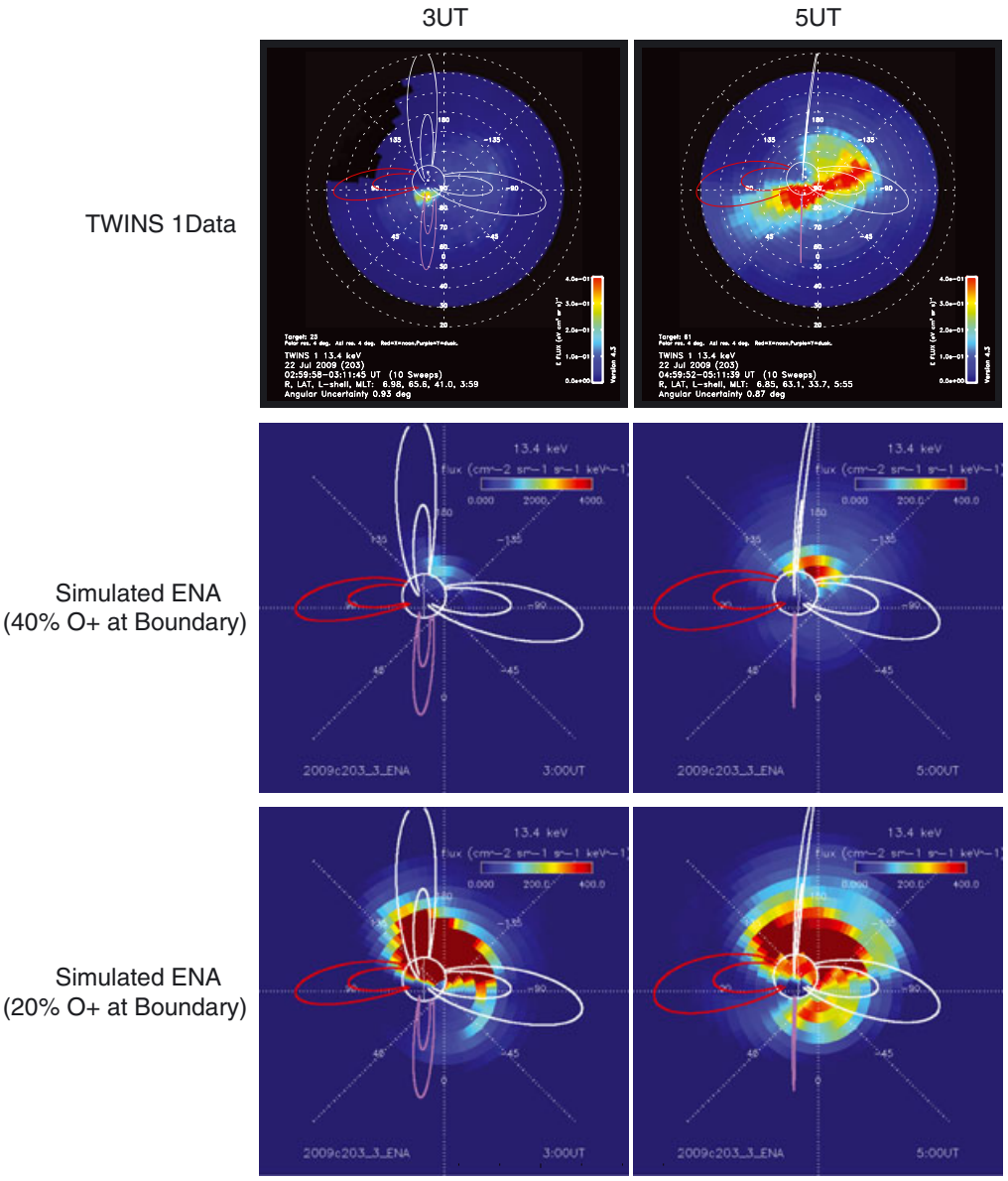

Figure 11. A comparison of observed and modeled ENA around 13.4 keV for 3:00 UT (left) and 5:00 UT (right). TWINS 1 observations are shown in the top row, the second row presents model results for the high O^+ case, and the bottom row presents model results for the low O^+ case.

are shown, 3:00 UT (left column) corresponding to a time as the Dst is dropping, and 5:00 UT (right column), which is close to the minimum Dst. We see that the case with more O^+ on the boundary has ENA flux levels closer to the TWINS 1 observations, while the case with less O^+ overestimates the ENA flux by about an order of magnitude. Additionally, the ENA flux predicted by the model is shifted counter-clockwise by about 45°. There are two sources of this MLT shift. First, the bow-tie-like strong emission seen in the ENA images is an internal scattering effect of the intense low-altitude ENAs [*Valek et al.*, 2010]. Disregarding this strong emission in the data removes some of MLT difference between the data and model. The rest of the MLT difference is likely due to the weaker shielding (and resulting increased skewing) noted in the THEMIS D comparison earlier.

[54] There are two likely explanations for how the model could overestimate the ENA flux. First, the empirical model of the neutral exosphere could be too dense. This would result in a larger number of ENAs being created since more cold neutrals are available to charge exchange with hot ring current ions. The second possibility is that the ion flux calculated by the model is too large. In this scenario, the number of hot ring current ions available to charge exchange with cold neutrals is greater. The second scenario seems to be consistent with the in situ THEMIS D observations, presented in Figure 10, which indicate that the simulation with less O^+ on the boundary tends to overestimate the flux on the inbound leg of the orbit, while the simulation with more O^+ slightly underestimates the flux. Such a pattern appears to be present in the ENA

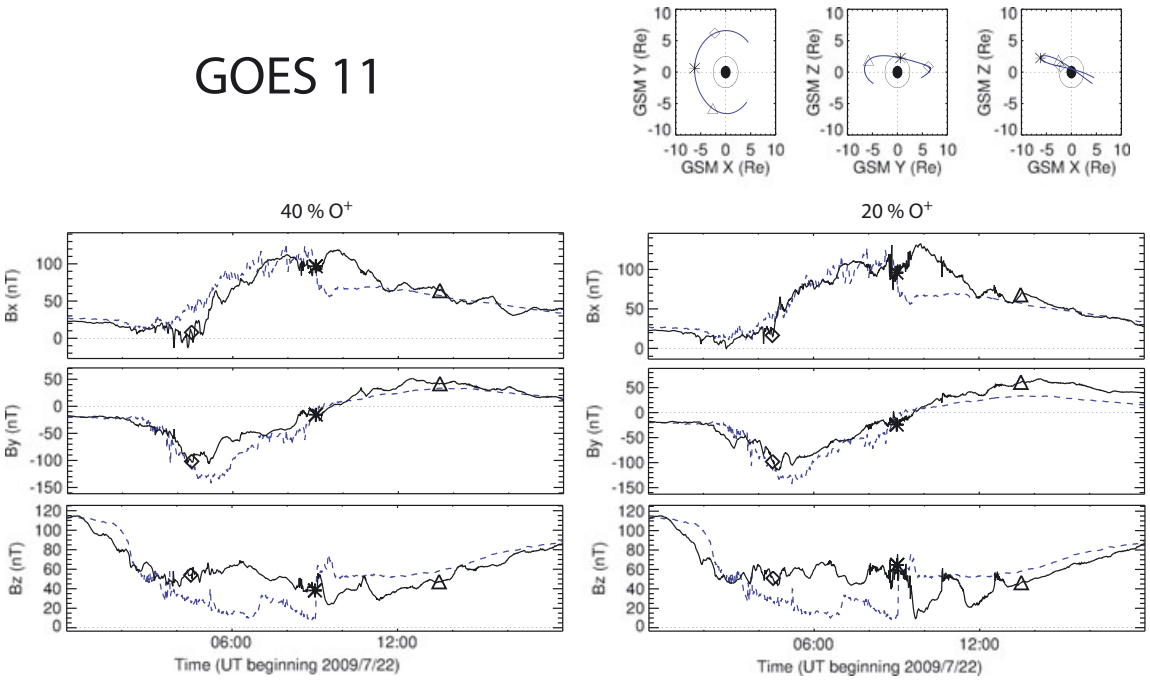

Figure 12. A comparison of simulated GOES 11 magnetic field data (black) with observations (blue) for the high O^+ case (left) and low O^+ case (right). The satellite trajectory is shown in the upper right.

comparisons as well, with the observed ENA flux being much closer to the simulation case with more O^+.

[55] It is tempting at this point to assume, based on the ion and ENA flux comparisons, that the amount of O^+ at the outer boundary of the inner magnetosphere must be close to 40% during this time. Caution must be taken, however, before drawing such a conclusion. For one thing, the Dst during the expansion and main phase of the event is closer to the case with less O^+. More importantly, the limitations of our model constrain us to make an assumption of not only the relative composition but the relative temperature as well. In these simulations, we assumed that the H^+ and O^+

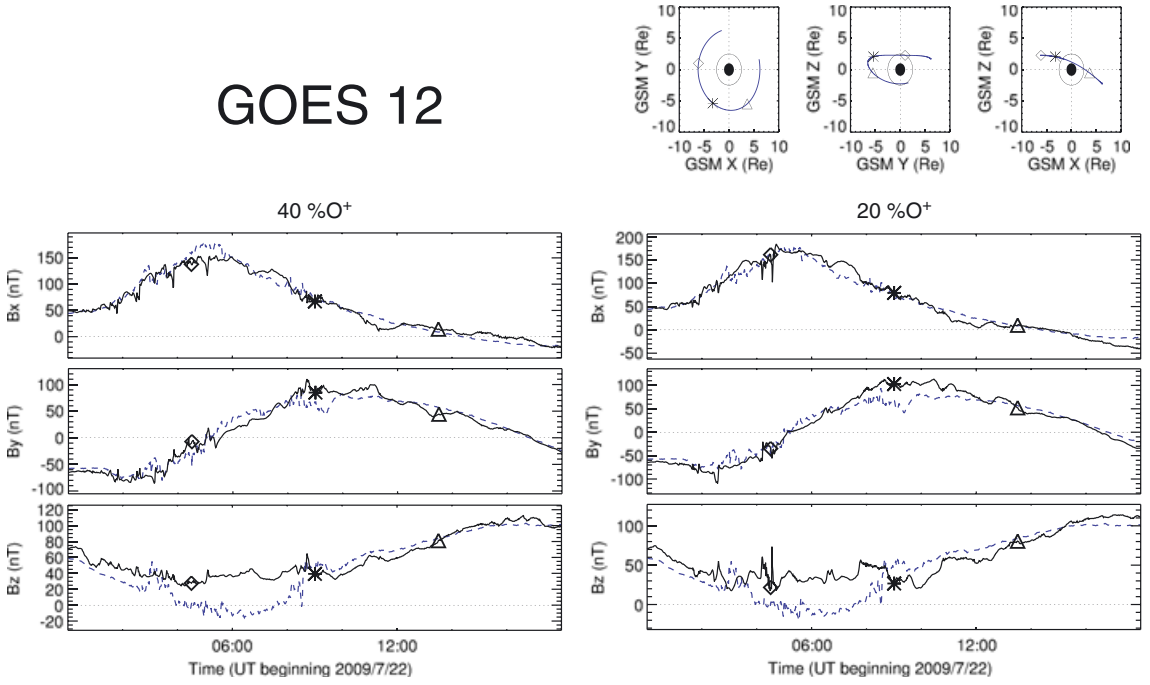

Figure 13. A comparison of simulated GOES 12 magnetic field data (black) with observations (blue) for the high O^+ case (left) and low O^+ case (right). The satellite trajectory is shown in the upper right.

temperatures are the same. As mentioned earlier, changing the relative temperature could affect the results, but such an investigation is beyond the scope of the current study.

[56] Our final data-model comparisons for this event look at the magnetic field at geosynchronous orbit as measured by the GOES 11 and 12 satellites. Figure 12 presents the comparison of the model to the GOES 11 satellite, and Figure 13 presents the comparison of the model to the GOES 12 satellite. In both figures, the upper right presents the satellite trajectory during the simulation; the plots on the left show the magnetic field components for the 40% O^+ case, while the plots on the right show the magnetic field components for the 20% O^+ case. The data are shown in blue, and the simulations are shown in black. Qualitatively speaking, both simulations do a reasonable job of capturing the magnetic field during the event with neither case performing obviously better than the other. One difference that does stand out is that the fluctuations in the modeled magnetic field appear stronger in the case with less O^+. This is particularly evident beginning around 9:00 UT in Figure 12. At this time GOES 11, located near midnight MLT, observes a significant dipolarization event with a sudden increase in B_Z. The modeled B_Z shows a jump in B_Z as well, albeit delayed in time. In comparing the two simulations, the variation is much stronger when less O^+ is present on the boundary.

[57] In contrast to the previous section which compared a single parameter, Dst, across multiple events, this section looked at various parameters for a single event. Overall, we found that the model does a reasonable job at replicating Dst, ion fluxes, and magnetic field. The overall ENA fluxes are consistent between the model and observations, but significant differences are visible. Moreover, we found that magnetospheric composition is a critical component that must be considered to appropriately model the inner magnetosphere.

4. Discussion and Conclusion

[58] We presented details and initial validation of the two-way coupled CRCM + BATS-R-US model; BATS-R-US represents the global magnetosphere, while CRCM represents the inner magnetosphere. Our coupling paradigm takes advantage of existing infrastructure in the SWMF for inner-magnetosphere coupling. Such reuse of coupling infrastructure for multiple modeling components with minimal software change is a key advantage of the framework approach. We used our newly coupled model to look at two studies: the ability to reproduce Dst for a range of events from the GEM Dst challenge and a detailed event study of the 22 July 2009 storm.

[59] In simulating the four events from the GEM Dst challenge, we were able to quantify model performance for events ranging from moderate to super storms. Dst is a nice parameter to focus on for multiple event validation of our model as it is related to the total energy density of the ring current. We found that our newly coupled model did a reasonable job predicting Dst and Sym-H according to our two metrics, prediction efficiency and predicted yield. The predictive yield demonstrated that we capture the net change in most cases within 20–30%. We also found a positive prediction efficiency for most cases without including a baseline shift in the modeled Dst and for all cases when the baseline shift was included. Moreover, we detailed two methods for calculating the Dst from the simulation, both of which give comparable results. As described in a forthcoming paper on the GEM challenge, coupled models, including this one, tended to perform favorably as compared to other global MHD models that did not include ring current coupling.

[60] Our second study focused on an event study of the 22 July 2009 geomagnetic storm. We simulated the event with our newly coupled model for two composition scenarios and directly compared the result with Dst, THEMIS D energy spectragrams, TWINS ENA images, and GOES 11 and 12 magnetometer data. Overall, we found that the model did an adequate job of replicating the trends in the data. We further found that composition can have a large effect on the result. Increasing the relative O^+ percentage on the CRCM outer boundary resulted in less ion flux being captured into the ring current. This resulted in lower Dst, lower differential energy flux, and reduced ENA emissions.

[61] It is important to note that lack of composition information is an inherent shortcoming of using single-fluid MHD for the global magnetosphere. Such a model is incapable of providing a specification of composition to the ring current model. We note that uncoupled ring current models also suffer from this issue. Therefore, we had to make assumptions regarding partitioning the density. Moreover, we assumed that O^+ and H^+ would have the same temperature at the boundary, but this is not necessarily true. Indeed, if the O^+ reaching the outer boundary was cold, it would be more likely to be captured and could result in a stronger ring current. As a result, we should be careful in interpreting the model results and not draw to a broad conclusion regarding the effect of composition. Moreover, future work should move toward using multifluid MHD representations of the global magnetosphere together with a specification of the ionospheric outflow.

[62] It is interesting to compare our results with recently published results from two-way coupled MHD LFM-RCM model [*Pembroke et al.*, 2012]. Under southward IMF Bz, the coupled model produced strong oscillations of the near-Earth plasma sheet and sawtooth signatures at geosynchronous orbit. To avoid instabilities, boundary between the RCM and LFM was placed inside 6 R_E. Our coupling scheme allows the boundary to be placed further from the Earth, to the CRCM typical boundary at $\sim$ 10 R_E. We do not find strong oscillations of the near-Earth plasma sheet as found by *Pembroke et al.* [2012]; still we have good data-model comparisons. The validity of the bounce-averaged approach to model dynamics of inner plasma sheet and particle injection was studied recently by *Wolf et al.* [2012a, 2012b]. It was shown that both the MHD and bounce-averaged approaches give a similar time integral of $E \times B$ drift velocity and net energization of the injection, although bounce-averaging misses some important aspects of physics (e.g., interchange oscillations). Based on these findings as well as on our results from data-model comparison, we conclude that our coupling scheme works reasonably well and allows us to describe the overall dynamics of the inner magnetosphere and near-Earth plasma sheet during storm times (although possibly missing some details of substorm injection).

[63] Overall, our newly coupled model demonstrated reasonable agreement with Dst, in situ, and remote

observations. Composition and its treatment was also found to be a very important consideration when including a ring current model into a global framework. Future improvements to this coupling scheme will include the use of a multifluid MHD code with an ionospheric source [*Glocer et al.*, 2009b] to represent the global magnetosphere and inclusion of pitch-angle anisotropy in the model coupling by using an anisotropic MHD code [*Meng et al.*, 2012].

[64] **Acknowledgments.** Resources supporting this work were provided by the NASA High-End Computing (HEC) Program through the NASA Advanced Supercomputing (NAS) Division at Ames Research Center and the NASA Center for Climate Simulation (NCCS) at Goddard Space Flight Center. This work was carried out as a part of the TWINS mission, which is part of NASA's Explorer Program.

References

Buzulukova, N., and V. Vovchenko (2008), Modeling of proton nose structures in the inner magnetosphere with a self-consistent electric field model, *J. Atmos. Sol. Terr. Phys.*, *70*, 503–510, doi:10.1016/j.jastp.2007.08.028.

Buzulukova, N., M.-C. Fok, J. Goldstein, P. Valek, D. J. McComas, and P. C. Brandt (2010), Ring current dynamics in moderate and strong storms: Comparative analysis of TWINS and IMAGE/HENA data with the Comprehensive Ring Current Model, *J. Geophys. Res. Space Phys.*, *115*, A12234, doi:10.1029/2010JA015292.

Buzulukova, N., M.-C. Fok, A. Pulkinnen, M. Kuznetsova, T. Moore, A. Glocer, P. Brandt, G. Toth, and L. Rastatter (2010), Dynamics of ring current and electric fields in the inner magnetosphere during disturbed periods: CRCM-BATSRUS coupled model, *J. Geophys. Res.*, *115*, A05,210, doi:10.1029/2009JA014621.

Buzulukova, N. Y., R. A. Kovrazhkin, A. L. Glazunov, J.-A. Sauvaud, N. Y. Ganushkina, and T. I. Pulkkinen (2003), Stationary nose structures of protons in the inner magnetosphere: Observations by the ion instrument onboard the Interball-2 satellite and modeling, *Cosmic Res.*, *41*, 3–12.

Cornwall, J. M., F. V. Coroniti, and R. M. Thorne (1970), Turbulent loss of ring current protons, *J. Geophys. Res.*, *75* (25), 4699–4709, doi:10.1029/JA075i025p04699.

De Zeeuw, D., S. Sazykin, R. Wolf, T. Gombosi, A. Ridley, and G. Tóth (2004), Coupling of a global MHD code and an inner magnetosphere model: Initial results, *J. Geophys. Res.*, *109* (A12), A12,219, doi:10.1029/2003JA010,366.

Dessler, A. J., and E. N. Parker (1959), Hydromagnetic theory of geomagnetic storms, *J. Geophys. Res.*, *64*, 2239–2252, doi:10.1029/JZ064i012p02239.

Fok, M.-C., and T. E. Moore (1997), Ring current modeling in a realistic magnetic field configuration, *Geophys. Res. Lett.*, *24*(14), 1775–1778.

Fok, M., T. E. Moore, and M. E. Greenspan (1996), Ring current development during storm main phase, *J. Geophys. Res.*, *101*, 15,311–15,322, doi:10.1029/96JA01274.

Fok, M., R. A. Wolf, R. W. Spiro, and T. E. Moore (2001), Comprehensive computational model of Earth's ring current, *J. Geophys. Res.*, *106*, 8417–8424, doi:10.1029/2000JA000235.

Fok, M., T. E. Moore, J. U. Kozyra, G. C. Ho, and D. C. Hamilton (1995), Three-dimensional ring current decay model, *J. Geophys. Res.*, *100*, 9619–9632.

Fok, M.-C., N. Buzulukova, S.-H. Chen, P. W. Valek, J. Goldstein, and D. J. McComas (2010), Simulation and TWINS observations of the 22 July 2009 storm, *J. Geophys. Res. A: Space Phys.*, *115*, A12231, doi:10.1029/2010JA015443.

Glocer, A., G. Tóth, T. Gombosi, and D. Welling (2009a), Modeling ionospheric outflows and their impact on the magnetosphere, initial results, *J. Geophys. Res.*, *114*, A05216, doi:10.1029/2009JA014053.

Glocer, A., G. Tóth, Y. Ma, T. Gombosi, J.-C. Zhang, and L. M. Kistler (2009b), Multifluid Block-Adaptive-Tree Solar Wind Roe-Type Upwind Scheme: Magnetospheric composition and dynamics during geomagnetic storms—Initial results, *J. Geophys. Res. Space Phys.*, *114*, A12203, doi:10.1029/2009JA014418.

Glocer, A., G. Tóth, M. Fok, T. Gombosi, and M. Liemohn (2009c), Integration of the radiation belt environment model into the space weather modeling framework, *J. Atmos. Sol. Terr. Phys.*, *71*, 1653–1663, doi:10.1016/j.jastp.2009.01.003.

Glocer, A., M.-C. Fok, T. Nagai, G. Tóth, T. Guild, and J. Blake (2011), Rapid rebuilding of the outer radiation belt, *J. Geophys. Res. Space Phys.*, *116*, A09213, doi:10.1029/2011JA016516.

Gombosi, T. I., G. Tóth, D. L. De Zeeuw, K. C. Hansen, K. Kabin, and K. G. Powell (2001), Semi-relativistic magnetohydrodynamics and physics-based convergence acceleration, *J. Comput. Phys.*, *177*, 176–205.

Goodrich, C., A. Sussman, J. Lyon, M. Shay, and P. Cassak (2004), The CISM code coupling strategy, *J. Atmos. Sol.-Terr. Phys.*, *66*, 1469–1479.

Harel, M., R. A. Wolf, P. H. Reiff, R. W. Spiro, W. J. Burke, F. J. Rich, and M. Smiddy (1981), Quantitative simulation of a magnetospheric substorm 1, model logic and overview, *J. Geophys. Res.*, *86*, 2217–2241.

Jaggi, R. K., and R. A. Wolf (1973), Self-consistent calculation of the motion of a sheet of ions in the magnetosphere, *J. Geophys. Res.*, *78*, 2852–2866.

Jordanova, V. K., J. U. Kozyra, G. V. Khazanov, A. F. Nagy, C. E. Rasmussen, and M.-C. Fok (1994), A bounce-averaged kinetic model of the ring current ion population, *Geophys. Res. Lett.*, *21*, 2785–2788, doi:10.1029/94GL02695.

Langel, R. A., G. D. Mead, E. R. Lancaster, R. H. Estes, and E. B. Fabiano, (1980), Initial geomagnetic field model from Magsat vector data, *Geophys. Res. Lett.*, *7*, 793–796, doi:10.1029/GL007i010p00793.

Liemohn, M. W., J. U. Kozyra, V. K. Jordanova, G. V. Khazanov, M. F. Thomsen, and T. E. Cayton (1999), Analysis of early phase ring current recovery mechanisms during geomagnetic storms, *Geophys. Res. Lett.*, *26*, 2845–2849.

Ma, Y.-J., et al. (2007), 3D global multi-species Hall-MHD simulation of the Cassini T9 flyby, *Geophys. Res. Lett.*, *34*, L24S10, doi:10.1029/2007GL031627.

Meng, X., G. Tóth, M. W. Liemohn, T. I. Gombosi, and A. Runov (2012), Pressure anisotropy in global magnetospheric simulations: A magnetohydrodynamics model, *J. Geophys. Res. Space Phys.*, *117*, A08216, doi:10.1029/2012JA017791.

Pembroke, A., F. Toffoletto, S. Sazykin, M. Wiltberger, J. Lyon, V. Merkin, and P. Schmitt (2012), Initial results from a dynamic coupled magnetosphere-ionosphere-ring current model, *J. Geophys. Res. Space Phys.*, *117*, A02211, doi:10.1029/2011JA016979.

Rastätter, L., et al. (2013), Geospace environment modeling 2008–2009 challenge: Dst index, *Space Weather*, doi:10.1002/swe.20036, in press.

Ridley, A., T. Gombosi, and D. Dezeeuw (2004), Ionospheric control of the magnetosphere: Conductance, *Ann. Geophys.*, *22*, 567–584.

Ridley, A. J., and M. W. Liemohn (2002), A model-derived storm time asymmetric ring current driven electric field description, *J. Geophys. Res.*, *107*(A8), doi:10.1029/2001JA000051.

Sazykin, S. Y. (2000), Theoretical studies of penetration of magnetospheric electric fields to the ionosphere, Ph.D. thesis, Utah State University, Logan, Utah.

Smith, P. H., and R. A. Hoffman (1974), Direct observations in the dusk hours of the characteristics of the storm time ring current particles during the beginning of magnetic storms, *J. Geophys. Res.*, *79*, 966–971, doi:10.1029/JA079i007p00966.

Stout, Q. F., D. L. De Zeeuw, T. I. Gombosi, C. P. T. Groth, H. G. Marshall, and K. G. Powell (1997), *Adaptive Blocks: A High Performance Data Structure,* sc, pp. 57–71, Proceedings of the 1997 ACM/IEEE Conference on Supercomputing, San Jose, Calif.

Sugiura, M. (1973), Magnetospheric field morphology at magnetically quiet times, *Radio Sci.*, *8*, 921–927, doi:10.1029/RS008i011p00921.

Toffoletto, F., S. Sazykin, R. Spiro, and R. Wolf (2003), Inner magnetospheric modeling with the Rice Convection Model, *Space Sci. Rev.*, *107*, 175–196.

Toffoletto, F., S. Sazykin, R. Spiro, R. Wolf, and J. Lyon (2004), RCM meets LFM: Initial results of one-way coupling, *J. Atmos. Sol-Terr. Phys.*, *66*, 1361–1370.

Tóth, G., et al. (2005), Space weather modeling framework: A new tool for the space science community, *J. Geophys. Res.*, *110*, A12,226, doi:10.1029/2005JA011126.

Tóth, G., D. L. De Zeeuw, T. I. Gombosi, and K. G. Powell (2006), A parallel explicit/implicit time stepping scheme on block-adaptive grids, *J. Comput. Phys.*, *217*, 722–758, doi:10.1016/j.jcp.2006.01.029.

Tóth, G., Y. J. Ma, and T. I. Gombosi (2008), Hall magnetohydrodynamics on block adaptive grids, *J. Comput. Phys.*, *227*, 6967–6984, doi:10.1016/j.jcp.2008.04.010.

Tóth, G., et al. (2012), Adaptive numerical algorithms in space weather modeling, *J. Comput. Phys.*, *231*, 870–903, doi:10.1016/j.jcp.2011.02.006.

Tsyganenko, N. A., and T. Mukai (2003), Tail plasma sheet models derived from Geotail particle data, *J. Geophys. Res.*, *108*, A3, 1136, doi:10.1029/2002JA009707.

Tsyganenko, N. A., and D. Stern (1996), Modeling the global magnetic field of the large-scale Birkeland current systems, *J. Geophys. Res.*, *101*, 27,187–27,198.

Valek, P., P. C. Brandt, N. Buzulukova, M.-C. Fok, J. Goldstein, D. J. McComas, J. D. Perez, E. Roelof, and R. Skoug (2010), Evolution of low-altitude and ring current ENA emissions from a moderate

magnetospheric storm: Continuous and simultaneous TWINS observations, *J. Geophys. Res. Space Phys.*, *115*, A11209, doi:10.1029/2010JA015429.

Vasyliunas, V. M. (2006), Ionospheric and boundary contributions to the Dessler-Parker-Sckopke formula for Dst, *Ann. Geophys.*, *24*, 1085–1097, doi:10.5194/angeo-24-1085-2006.

Welling, D. T., and A. J. Ridley (2010), Validation of SWMF magnetic field and plasma, *Space Weather*, *8*, S03002, doi:10.1029/2009SW000494.

Welling, D. T., V. K. Jordanova, S. G. Zaharia, A. Glocer, and G. Toth (2011), The effects of dynamic ionospheric outflow on the ring current, *J. Geophys. Res. Space Phys.*, *116*, A00J19, doi:10.1029/2010JA015642.

Wolf, R. A., C. X. Chen, and F. R. Toffoletto (2012a), Thin filament simulations for Earth's plasma sheet: Interchange oscillations, *J. Geophys. Res. Space Phys.*, *117*, A02215, doi:10.1029/2011JA016971.

Wolf, R. A., C. X. Chen, and F. R. Toffoletto (2012b), Thin filament simulations for Earth's plasma sheet: Tests of validity of the quasi-static convection approximation, *J. Geophys. Res. Space Phys.*, *117*, A02216, doi:10.1029/2011JA016972.

Young, D. T., H. Balsiger, and J. Geiss (1982), Correlations of magnetospheric ion composition with geomagnetic and solar activity, *J. Geophys. Res.*, *87*, 9077–9096.

Zaharia, S., V. K. Jordanova, M. F. Thomsen, and G. D. Reeves (2006), Self-consistent modeling of magnetic fields and plasmas in the inner magnetosphere: Application to a geomagnetic storm, *J. Geophys. Res. Space Phys.*, *111*, A11S14, doi:10.1029/2006JA011619.

Zaharia, S., V. K. Jordanova, M. F. Thomsen, and G. D. Reeves (2008), Self-consistent geomagnetic storm simulation: The role of the induced electric fields, *J. Atmos. Sol. Terr. Phys.*, *70*, 511–518, doi:10.1016/j.jastp.2007.08.067.

Zaharia, S., V. K. Jordanova, D. Welling, and G. Tóth (2010), Self-consistent inner magnetosphere simulation driven by a global MHD model, *J. Geophys. Res. Space Phys.*, *115*, A12228, doi:10.1029/2010JA015915.

Zhang, J., et al. (2007), Understanding storm-time ring current development through data-model comparisons of a moderate storm, *J. Geophys. Res.*, *112*, A04,208, doi:10.1029/2006JA011,846.